Energy & Environmental Science

ROYAL SOCIETY OF CHEMISTRY

PAPER

View Article Online
View Journal | View Issue

Cite this: *Energy Environ. Sci.*, 2026, **19**, 3236

Reconstructing the electrochemistry of lithium-ion batteries through *operando* diffuse reflectance spectroscopy

Arvind Pujari, *[abc] Gratsiela Kostova, [b] Hwee Jien Tan, [b] Atsunori Ikezawa, [c] Hajime Arai [c] and Michael De Volder *[b]

Received 18th January 2026,
Accepted 8th April 2026

DOI: 10.1039/d6ee00376a

rsc.li/ees

Studying batteries in real time is essential for understanding their operation and degradation mechanisms. *Operando* methods such as X-ray diffraction, NMR, and electron microscopy provide detailed insights but are costly, complex, and require specialized cell designs, making them impractical for long-term cycling or screening. Here, we propose using *operando* diffuse reflectance spectroscopy (DRS) to probe battery electrodes as they charge and discharge. This technique measures subtle changes in the reflectance spectrum of battery electrodes caused by electronic structure changes during cycling. By correlating these optical property changes with the state-of-charge of the battery, we can reconstruct a 'second view' of the electrochemistry of the battery. We show that DRS can be used to determine heterogeneity in state-of-charge, study solid state lithium-ion diffusion, uncover the origin of first cycle capacity losses, and study surface limited behaviour. We apply *operando* DRS to a wide variety of battery materials to show that the proposed method enables the extraction of information that previously was only accessible using methods that are orders of magnitude more expensive.

Broader context

Understanding how batteries function and degrade under realistic operating conditions is central to improving their performance, lifetime, and safety. *Operando* characterization techniques such as X-ray diffraction, nuclear magnetic resonance, and electron microscopy have played a key role in studying battery operation, but these techniques do not allow for easy parallel screening of batteries or long-term studies. Developing compact and cost-effective *operando* analysis methods that allow for testing different electrochemical conditions is crucial going forward. Here, we introduce *operando* diffuse reflectance spectroscopy (DRS) as a new, low-cost technique to probe lithium-ion batteries. By measuring changes in reflected light from the surface of battery electrodes as a function of state of charge, we show that DRS can be used to obtain information about oxidation state changes, electrode heterogeneity, solid state diffusion, and the origins of battery degradation. The ability to extract rich electrochemical and materials information using this simple optical measurement opens new opportunities for high throughput screening, long-term degradation studies, and accelerated development of next-generation battery materials.

Introduction

The growing need for electrification has increased demand for lithium-ion batteries in grid storage and electric vehicles. 'Looking inside' batteries through *operando* techniques that monitor batteries during charge and discharge can reveal how they function, degrade, and can be improved. Methods such as synchrotron X-ray spectroscopy,[1–3] nuclear magnetic resonance (NMR),[4–6] mass spectroscopy,[7,8] Raman spectroscopy,[9–13] and electron microscopy[14–16] have provided valuable insights, but are costly, complex, and often require specialized cell designs. This makes them impractical for long-term degradation studies, high-throughput screening, or experimental replicates needed to account for cell-to-cell variation. Their expense also limits accessibility in developing countries.[17] Thus, low-cost *operando* methods are essential for scalable studies and democratizing battery research.

Recent developments in optical battery characterization exploit correlations between electrode particle reflectance and state of charge. Reflection[18,19] and confocal microscopy[20,21] techniques have provided new insights into Li-ion battery operation by monitoring brightness changes in electrodes/battery particles during cycling. During lithium deintercalation, increased conduction band electron population increases material polarizability, resulting in higher light scattering and reflectance, with the opposite occurring during intercalation.[22]

[a] *Cavendish Laboratory, Department of Physics, University of Cambridge, CB3 0HE, UK. E-mail: ap2180@cam.ac.uk*
[b] *Institute for Manufacturing, Department of Engineering, University of Cambridge, CB3 0FS, UK. E-mail: mfld2@cam.ac.uk*
[c] *School of Materials and Chemical Technology, Institute of Science Tokyo, Tokyo, 226-8502, Japan*

Fig. S1(a) demonstrates this principle through *operando* cross-sectional confocal microscopy of an $LiFePO_4$–Li half-cell, where electrode brightness increased during charging and decreased during discharge.[23] However, microscope components such as lenses, autofocus setups, and motorized stages are usually expensive. Moreover, microscope objectives cannot collect all the reflected light (this is dependent on the size of aperture used), which leads to issues when detecting subtle reflectance changes, and can only image a small part of the cell, leading to issues in statistical significance (Note S1 and Fig. S2). Consequently, a technique to efficiently capture reflectance changes in batteries without the complexities associated with imaging could be an easy to use, inexpensive technique to probe batteries in real time. Thus, we introduce *operando* diffuse reflectance spectroscopy as a cost-effective alternative for optical battery characterization allowing for the sensitive, real-time detection of battery reflectance.

A setup for *operando* diffuse reflectance spectroscopy of lithium-ion batteries

When polychromatic light is incident on a surface, it can undergo specular reflection (mirror-like, from smooth surfaces) or diffuse reflection (scattered in multiple directions from rough surfaces) as shown in Fig. 1(a) and Fig. S3. In optically accessible batteries, the glass window produces specular reflections while the rough cathode powder results in diffuse reflection. As the SoC of the battery changes, the nature and intensity of light reflected by the electrode changes. Previous approaches[24,25] to track the reflectance of batteries have used optical fibres to track specular reflectance. However, they mainly used thin film electrodes, which suffered from poor signal collection efficiency, and required non-standard cell formats, limiting their practical applicability (Note S1). Thus, there is a need to develop diffuse reflectance setups that measure reflectance data over large electrode areas without drastically modifying the cell format and temperature.

To do this we use a setup consisting of an integrating sphere, tungsten-halogen light source, charge coupled device (CCD) spectrometer, and an optical coin cell, as shown in Fig. 1(b). This approach does not require any lenses or other optical components and averages a response over the entire illuminated area (9 mm diameter window in our case), *i.e.* thousands of particles. A detailed description of our setup can be found in the Methods and Note S3, with a digital image provided in Fig. S4. Briefly, the integrating sphere uses a highly reflective spherical cavity with a gloss trap to selectively collect

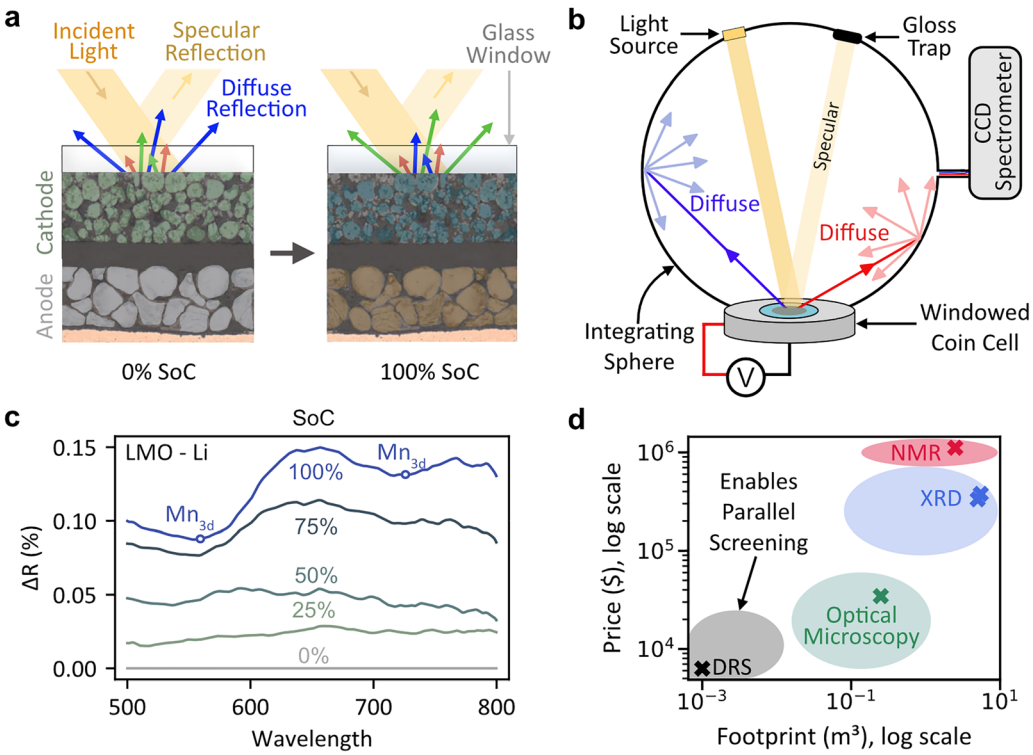

Fig. 1 Setup for the *operando* monitoring of the reflectance of battery electrodes. (a) When light is incident on a surface two types of reflection are usually obtained: specular – where the angle of incidence is equal to the angle of reflectance (*e.g.*, a polished surface such as a glass window), and diffuse – where incident light is scattered in different directions (*e.g.*, a rough surface such as a battery electrode). The light reflected by a battery electrode also changes as a function of SoC. (b) In this study, a windowed coin cell is mounted on an integrating sphere. White light is incident on the coin cell. Specular reflection (from the glass window) is eliminated through a gloss trap while scattered diffuse light (from the electrode) undergoes Lambertian reflection in the sphere until it enters the optical fibre leading to the spectrometer. (c) The reflectance spectrum of LMO *vs.* Li at different SoCs, with reference to the spectrum at 0% SoC. The reflectance troughs (or absorption peaks) seen at 560 nm and 725 nm for LMO have been previously reported as corresponding to electronic transition between Mn_{3d} states. (d) Comparing the cost and footprint of DRS with other major *operando* techniques such as NMR, XRD, and optical microscopy. The lower cost and footprint of DRS could enable parallel screening of several cells under (temperature) controlled conditions, as shown in the left sketch.

diffuse reflectance from the electrode while excluding specular reflections from the glass window. Since cathode materials and carbon additives absorb most incident light, the resulting diffuse reflectance changes are subtle (1–3%), requiring the sphere's high collection efficiency to detect these small spectral variations. We use optically accessible coin cells with either a transparent fluorine-doped tin oxide (FTO) current collector in a configuration similar to conventional coin cells (transmissive configuration) or with an aluminium mesh current collector between the separator and freestanding electrode (non-transmissive configuration). In both cases, due to the limited optical penetration depth of light the region of the electrode probed is the part closest to the glass window and furthest away from the separator, which we refer to as the 'bottom' of the electrode. Further information about the coin cells used in this study can be found in Note S4 and Fig. S5. We note that the modified parts of the coin cell (casing with hole, glass window, sealing thermoplastic, protective epoxy, stainless steel mesh) are commercially available with further details in the Materials and Methods section. The cell is mounted on the integrating sphere *via* a 3D printed mount with a spring-loaded pin contact. We have previously established that our modified coin cells with free standing electrodes provide standard stack pressures, and electrochemical performance/overpotentials comparable to conventional coin cells even at high rates and over several cycles.[26,27]

By collecting diffuse reflectance spectra of the electrode as a function of SoC, we reconstruct the electrochemistry of the battery, enabling a 'second view' of the SoC of the battery, with an acquisition time of <10 s. Due to the low optical penetration depth of most cathodes, the optical penetration depth of DRS is of the orders of hundreds of nanometres ($\sim$100 nm for $LiMn_2O_4$[28] (LMO) or $\sim$217 nm for $LiFePO_4$[29]) classifying it as a subsurface technique. To validate the proposed technique, we begin by documenting the changes in diffuse reflectance spectrum as a function of SoC for LMO when it is cycled against an Li metal anode in Fig. 1(c). The spectra shown here are with respect to the spectrum at 0% SoC, and the raw spectra (before subtraction) can be found in Fig. S9c and d. Notably, the reflectance at all wavelengths increases with SoC as the material polarizability changes, as discussed previously. LMO is well known to undergo both a solid solution and phase change reaction during the first and second charging plateau respectively, highlighting that different reaction mechanisms can elicit a change in reflectance. Additionally, reflectance peaks and troughs emerge at higher SoCs. As reflectance can viewed as the complement of absorbance, the troughs at 550 nm and 720 nm indicate absorbance peaks, corresponding to O-2p to Mn-d electronic transitions.[30,31] The large jump in reflectance at $\sim$50% SoC is due to a phase change which results in the formation of an MnO_2 shell.[32] Thus, DRS can track changes in the reflectance of battery materials (which is correlated to its SoC) and oxidation changes occurring during charge/discharge.

The proposed DRS setups can be assembled from individual components as described above or mounted on commonly available UV-VIS tools. By reducing the number of components required, we drastically reduce the cost of our system with respect to optical microscopy, and other *operando* techniques such as NMR and XRD (Fig. 1(d) and Table S1). The low-cost and footprint of DRS could allow for the parallel screening of several cells under controlled conditions (for instance up to six DRS setups could be placed in a normal-sized climate chamber), enabling statistically significant *operando* studies.

To highlight the several use cases for DRS in battery research, in this report we demonstrate the ability to (i) reconstruct the electrode SoC during charge and discharge, (ii) study reaction heterogeneity across the depth of porous electrodes at different charging rates, (iii) recreate and complement cyclic voltammetry plots as well as surface limited behaviour (iv) study first-cycle capacity losses in systems limited by solid state diffusion, and (v) analyse the origins of capacity loss in the initial cycles of nickel rich cathodes as well as surface degradation.

Reconstructing electrochemistry through *operando* DRS

We next show how DRS can be used to recreate electrochemical phenomena in a range of popular battery chemistries including LFP, LMO and NMC811 cathodes (all measured at 0.15–0.2C in half cells in the non-transmissive configuration).[32–34]

Fig. 2(a–d) demonstrates a more intuitive representation of the plots in Fig. 1(c): change in reflectance *vs.* time/SOC for several battery materials. Each line represents the change in reflectance at a specific wavelength *vs.* time (*e.g.*, the blue line shows ΔR for LFP at 500 nm *vs.* time). All three cathode materials ($LiFePO_4$, NMC811, $LiMn_2O_4$ exhibit reversible reflectance changes during cycling, demonstrating broad applicability across olivine, layered, and spinel structures. However, reaction mechanisms create subtle differences: while all three cathodes become more reflective when charged, LFP and NMC show maximum changes at short wavelengths, whereas LMO displays maximum changes in reflectance at long wavelengths. In the case of an anode material (TiO_2, Fig. 2(d)), the reflectance of the battery decreases as lithium ions are intercalated into the crystal structure.

To compare reflectance changes across wavelengths, we normalize each wavelength's change in reflectance *vs.* time plot by its maximum change. The normalized plots for LFP (Fig. S7(b)) show consistent rates of increase/decrease across 500–800 nm, indicating wavelength-independent reflectance *vs.* SoC behaviour. This is because during LFP's two-phase reaction, both FP ($FePO_4$) and LFP coexist, and the resultant spectrum is a combination of their optical properties. Fig. S8 plots their reflectance change relative to the original spectrum. No visible peaks are seen as transitions corresponding to the Fe^{2+} and Fe^{3+} oxidation states absorb light in the ultraviolet region.[35] In contrast, NMC811 develops a visible reflectance peak at $\sim$620 nm during charging due to $Ni^{3+/4+}$ oxidation (Fig. S9(a) and (b)). This is confirmed by similar behaviour in its parent material $LiNiO_2$ (peak at $\sim$660 nm) with the absence of Co/Mn dopants causing the slight wavelength shift, Fig. S10). This wavelength-dependent response complicates optical microscopy imaging,[18,20] but DRS can guide optimal wavelength selection

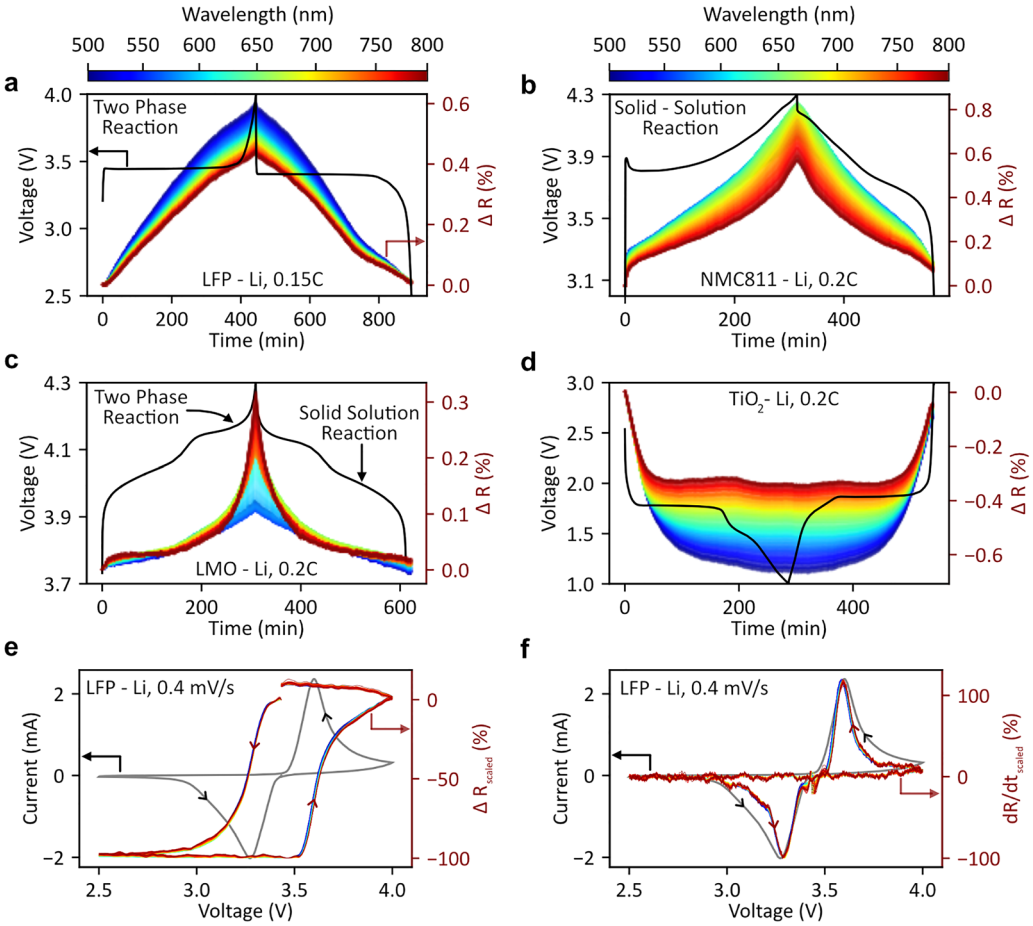

Fig. 2 Reconstruction of electrochemistry through DRS. Diffuse reflectance *vs.* time curves obtained during the charge/discharge of (a) $LiFePO_4$ *vs.* Li (a two-phase reaction). (b) NMC811 *vs.* Li (a solid solution reaction). (c) LMO *vs.* Li (solid solution + two-phase reaction). (d) TiO_2 *vs.* Li (two-phase reaction anode). (e) Voltage *vs.* current during a 0.4 mV s^{-1} CV scan of delithiated LFP (black) at 500 nm with the corresponding reflectance *vs.* time plots (grey) overlaid on it. (f) The same voltage *vs.* current plot (black) with the derivative of reflectance *vs.* time (d*R*/d*t*, red) overlaid on it. The d*R*/d*T* plot closely mirrors the CV plot. The variety of reversible spectra seen across different materials and reaction mechanisms highlights the wide applicability of this technique.

and establish reflectance-SOC calibration curves for materials which develop absorbance peaks at higher SoCs (Note S5).

We next show that DRS can be used to recreate CV curves (see Fig. 2(e) and (f)). At scan rate of 0.4 mV s^{-1} (Fig. 2(e)), LFP reflectance changes closely align with the CV oxidation/reduction peaks. Since changes in reflectance are strongly correlated with capacity, its derivative with respect to time serves as a current proxy. This enables the construction of 'optical CVs' (Fig. 2(f)). We performed electrochemical CVs at multiple rates (0.4–1 mV s^{-1}, Fig. S11) and constructed corresponding optical CVs. These CVs at different scan rates can be used to obtain '*b*-values', which are a measure of the extent of capacitive or diffusive contributions in an electrode.[36] Both electrochemical and optical CVs yield *b*-values of 0.5 (Fig. S13). A value of $b = 0.5$ is to be expected from the micron sized LFP particles used here, and confirms the intercalative behaviour seen. Obtaining the same value from the optical CVs strongly validates the optical CV reconstruction and highlights a potential use case for discerning between capacitive and diffusive contributions. However, particle refractive indices and lithiation/delithiation dynamics can introduce complexities into the interpretation of the curves. For instance, CV curves of NMC811 *vs.* Li (Fig. S12) show a correlation between electrochemical and optical CV curves during oxidation, with an offset seen during reduction, which may be attributed to the formation of a 'core–shell' structure due to poor lithiation dynamics at low SoCs.[19] Meanwhile an offset is seen during both the lithiation and delithiation of TiO_2 due to its high transmittivity, as discussed further along in the manuscript (Fig. 4).

The cells can be cycled several times while their reflectance spectra are recorded (demonstrated in subsequent sections), highlighting the reversibility of the changes in reflectance and the robustness of both the proposed DRS technique and optical cell design. Further, we test cell-to-cell reproducibility by comparing two coin cells with an identical configuration (NMC811 *vs.* Li) in Fig. S15. The electrochemistry and scaled reflectance *vs.* time plots of both sets of cells are remarkably similar, which is challenging to achieve with many *operando* techniques. It should be noted here that light source stability, thermal drift,

wetting, bubble formation and other factors can influence the observed DRS response and must be carefully accounted for, as indicated in Note S6 and Fig. S14.

Using an integrating sphere is essential because total reflectance (specular + diffuse) shows much weaker SoC-dependent changes due to dominant, unchanging specular reflection from the glass window, which saturates the spectrometer. This necessitates the use of lower integration times/averaging, leading to noisier data. This also explains why previous fibre optic and microscopy studies have reported non-monotonic or noisy reflectance changes (Fig. S16 and Note S7). Additionally, microscopy data reveals that different crystallographic orientations in single crystal particle reflect light differently during cycling, creating inhomogeneities that bias small-area measurements (Note S8 and Fig. S17). Our large-area diffuse reflectance approach averages out local inhomogeneities due to particle orientation out for more representative state-of-charge tracking.

Finally, although the data collected in this paper is based on a systems assembled in-house using commercially available parts, we demonstrate the proposed DRS battery analysis can also be carried out using commercial UV-vis integrating sphere for which we provide details in Fig. S18 and Note S9. Integrating spheres are available as add-ons for many commercial UV-vis spectrometers, and the ubiquitous nature of this tool within physical science laboratories positions DRS as a quick and accessible tool for battery research.

Studying electrode heterogeneity through DRS

We next use DRS to optically recreate various electrochemical phenomena. First, we study reaction heterogeneity by mapping lags in SoC at the bottom of LFP cathodes and show that the precise tracking of SoC at the current collector (here transparent FTO, transmissive configuration) through DRS during a rate test can help determine limiting processes at higher rates.

We cycle two cathodes with identical compositions but differing mass loadings (4 mg cm^{-2} and 23 mg cm^{-2}) and classify them as 'thin' and 'thick' respectively. The cells are charged and discharged at different rates (0.15C, 0.5C, 0.8C, 1C, 2C, 3C, and 4C) consecutively. Given the uniform diffuse reflectance *vs.* time plots of LFP (as highlighted in the previous section) we use the reflectance at 500 nm for all analysis, as the choice of wavelength is inconsequential. The scaled reflectance *vs.* time plots for the thin and thick electrodes at different rates are shown in Fig. S19(a) and (b) respectively. As the rate increases the peak reflectance reached decreases, as is expected from the capacity decrease with increasing rate. This shows that DRS data can be recorded for extended time periods with high temporal resolution. The capacity at different rates for both sets of electrodes is shown in Fig. S20 with the corresponding changes in reflectance plotted alongside, again highlighting the correlation between SoC and reflectance.

There are interesting differences in the linearity of the reflectance *vs.* time plots between the thick and thin electrodes Fig. 3(a) and (b). It is important to note here that due to the limited optical penetration depth of light, the reflectance seen corresponds to the electrochemistry of the bottom of the electrode (near the current collector, farthest from separator), *i.e.* the region with worst ion transport limitations. We validate this with optical transport simulations of the electrode which also take into account scattering and other components of the electrode and show that the penetration depth of light within the electrode never exceeds a few micron (Fig. S20). DRS thus reconstructs electrochemistry in the most diffusion-limited zone, enabling identification of mass transport constraints (see cross-sectional confocal microscopy Fig. S22 and Note S10).

During charging (Fig. 3(a and b)), the thick electrode shows lower capacity but similar average potential to the thin electrode, making it impossible to identify the limiting factor from electrochemistry alone. Looking at the reflectance *vs.* time plots provides additional clues. In the case of the thin LFP electrode (Fig. 3(a)), the increase in reflectance with time is roughly linear during the charge and linear during the discharge. This implies that the SoC of the electrode (in this case the region furthest away from the separator) increases uniformly with time. This suggests that there are no transport limitations making the SoC at the bottom of the electrode deviate from the average electrode SoC.

However, for the thick electrode, the reflectance *vs.* time plots are not linear, and are instead convex during the charging process and concave during the discharging process (Fig. 3(b)). This indicates that both the charging and discharging processes at the bottom of the electrode proceed at a slower rate than electrode average (SOC increases linearly with time in galvanostatic experiments) due to mass transport limitations across the depth of the electrode. A closer look reveals that for the first 10 minutes of the charging process there is very slow increase in reflectance, suggesting that it takes a significant amount of time for the bottom of the electrode to start delithiating. The same is true for the discharging process, where a lag in SoC change and slow rate of reaction (RoR) is also observed at the bottom of the electrode. This information is not readily available from electrochemical profiles – thus DRS is a powerful method to understand electrode heterogeneity. The reflectance of the thick LFP electrode increases rapidly at the end of charge (discharge), suggesting that the bottom of the electrode is playing 'catch-up' when the parts of the cathode closer to the separator are fully delithiated (lithiated). In general, the deviation from a slow rate reflectance *vs.* time plot can be used as a 'quality' factor for SoC heterogeneity across the electrode.

Further, shifts in reflectance (or in other words SoC) during rate tests inform how much capacity is lost on the charge and discharge process at high rates. For this, we plot the maximum and the minimum reflectance for each cycle in Fig. 3(c) and (d), which enables us to track the SoC of the cathode surface at both the top and bottom of charge. For the thin electrodes, the maximum reflectance reached constantly decreases while the minimum reflectance reached slightly increases, *i.e.* mass transport limitations during delithiation cause the decrease in capacity at higher rates. For the thick electrodes (Fig. 3(d)), the maximum reflectance reached decreases rapidly at higher rates. Additionally, we observe that for high rates of 2C and

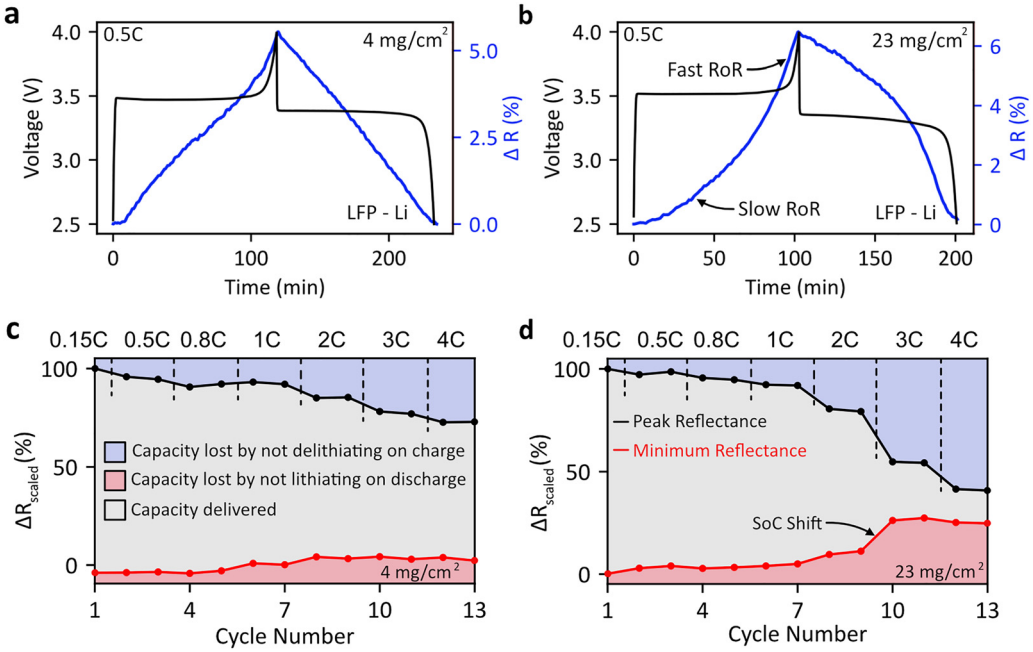

Fig. 3 DRS based heterogeneity analysis of thin (4 mg cm^{-2}) and thick (23 mg cm^{-2}) LFP electrodes. (a) The corresponding reflectance vs time profiles during the 0.5C charge discharge cycle for the thin electrode. A reasonably linear increase/decrease in reflectance can be seen with time, suggesting that the rate of reaction proceeds uniformly at all SoCs. (b) The corresponding reflectance *vs.* time profiles during the 0.5C charge discharge cycle for the thick electrode. The increase in reflectance at the start of charge is slow, suggesting a low rate of reaction (RoR) due to mass transport limitations – information that cannot easily be gleaned through electrochemistry. (c) Variation of peak and minimum reflectance at 500 nm recorded during the cycling of the thin LFP electrode. (d) Variation of peak and minimum reflectance at 500 nm recorded during the cycling of the thick LFP electrode. A 'shift' in SoC, resulting in a lower charge SoC and higher discharge SoC is observed.

above, the electrode surface reflectance does not return to its minimum reflectance, indicating that the battery does not return to its fully lithiated state. Thus, poor kinetics at during both charge and discharge (above 2C) are responsible for the reduction in capacities at higher rates. Hence, DRS enables us to deconvolute electrode level kinetic limitations and shifts in SoC that cannot be extracted from the battery voltage only.

Probing surface reactivity and phase propagation through optical CVs

As described above, DRS can be used to optically reconstruct the CV curves of LFP, with the optical and electrochemical peak positions coinciding. Subtle differences emerge depending on light's optical penetration depth into the material, which we will demonstrate using anatase TiO_2.[37]

Fig. 4(a) and Fig. S23(b) show electrochemical and optical CV curves at 0.4 mV s^{-1} for anatase-TiO_2 cycled against Li metal. While both curves display similar features with large oxidative and reductive peaks, the peak positions do not coincide – both reflectance 'current' peaks occur after their electrochemical counterparts. This trend persists across all scan rates tested (0.1–5 mV s^{-1}, Fig. S23). Fig. 4(b) quantifies the voltage offset *versus* scan rate, revealing two key trends: the oxidation peak offset is smaller than the reduction peak offset, and both offsets increase with scan rate. This does not occur in the case of LFP Fig. 4(c). Fig. 4(d) illustrates why this occurs. While DRS is typically surface-sensitive due to low optical penetration depths in most cathodes, TiO_2 is a semiconductor with a ~3.2 eV band gap (~388 nm), thus it has high transmittance at the spectroscopy wavelengths used (500–800 nm). Upon lithiation, however, optical transmissivity and reflectance decrease as the conduction band (mainly Ti-3d orbitals with O-2p admixture) fills.[38,39] This electrochromic behavior[40] causes TiO_2 to change from transparent to dark blue during lithiation.

The phase front in anatase TiO_2 propagates from the surface,[41] creating concentration gradients between surface and core due to poor solid-state diffusion. As shown in Fig. 4(d), a Li_xTiO_2 phase forms at the particle surface. Since Li_xTiO_2 has much lower optical transmittance than TiO_2 (even at small x values),[41] the reflectance drops sharply before bulk lithiation occurs. Consequently, the dR/dt peaks appear earlier (at higher voltages) than the electrochemical peaks. At higher scan rates, lithiation becomes increasingly surface-limited,[42] creating a more lithium-rich surface phase and resulting in less bulk lithiation. This surface Li_xTiO_2 phase forms rapidly and is immediately detected by DRS. The greater surface-to-bulk Li_x-TiO_2 ratio at higher rates contributes to the wider offset between electrochemical and dR/dt reduction peaks.

During delithiation, the TiO_2 phase propagates from the surface (Fig. 4(d)). Since TiO_2 is transmissive, light penetrates to the less transmissive Li_xTiO_2 core until all bulk Li_xTiO_2 converts to TiO_2. Thus, the dR/dt peak is delayed until after bulk oxidation, occurring at higher voltage. However, the

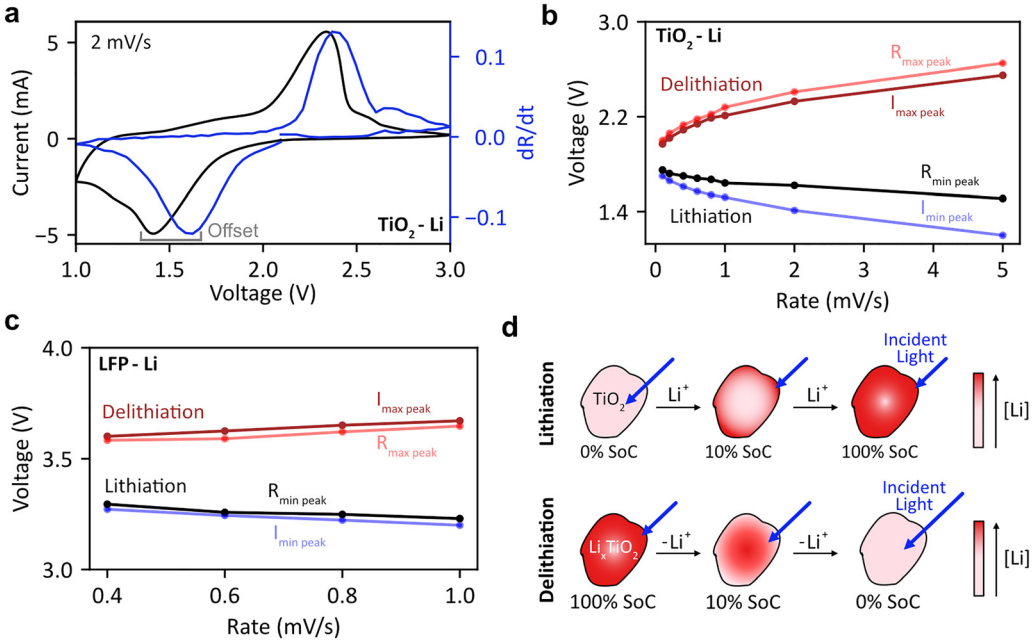

Fig. 4 Reconstruction of cyclic voltammetry curves through DRS. (a) Electrochemical and optical CV curves of TiO_2 *vs.* Li, at 2 mV s^{-1}. An offset between the peak positions of the two curves is seen. (b) Quantification of the offset between the reflectance and electrochemical plots. The offset is greater during lithiation and increases with increasing scan rates. (c) Quantification of the offset between the reflectance and electrochemical CV plots in LFP. Unlike the case of TiO_2, there is practically no offset between the electrochemical and optical CV curves. (d) An explanation of the difference in optically recreated CV plots and electrochemical CV plots. Differences in optical penetration depth (δ_p) of TiO_2 and Li_xTiO_2 lead to an offset in peak positions.

oxidation peak offset is more rate-independent than reduction peaks, suggesting bulk diffusion and not surface reactivity limits delithiation, likely due to the insulating TiO_2 shell restricting ionic and electronic transport. In contrast, for LFP (Fig. 4(c)), both FP and LFP phases have low optical penetration depth at 500–800 nm,[29] so optical reflectivity represents a combination of both phases, and optical and electrochemical peaks coincide.

In a broader context, this study shows that interesting information can be obtained from battery materials where the two phases have very different optical contrasts. Although this study focuses on using visible wavelengths, extending the range of DRS to the UV or IR could enable the study of other materials which exhibit significant optical contrasts (such as FP and LFP in the UV[29]).

Tracking Li-ion diffusion in cathode materials

In materials with poor solid-state diffusion, significant lithium concentration polarization can occur within particles which can manifest as capacity losses and poor rate performance. Here we show how the correlation between reflectance and SoC can be used to probe relaxation dynamics in NMC811 cathodes (in a non-transmissive cell configuration). Fig. 5(a). shows our electrochemical protocol consisting of a slow charge and discharge at 0.15C, followed by a faster 1C cycle, with a 5 hour open circuit voltage (OCV) rest after each cycle.

After the slow charge/discharge, both the cell voltage and reflectance increase during the 5 h rest, which is in agreement with Li inserted at the surface of the particles redistributing to the core of the NMC811 particles,[19] as shown in graphic under Fig. 5(a). This is because at low SoC (high degree of lithiation) the solid-state lithium-ion diffusion coefficient in NMC811 drops.[26] This results in preferential lithiation of the surface of the NMC811 particle (during discharge) while the bulk of the particle is less lithiated. During the OCV period, the concentration gradient within the particle equilibrates, and lithium diffuses from the surface to the core of the particle. This manifests as apparent delithiation of the surface of the particle, and hence an increase in the magnitude of reflectance. We reiterate that due to the ability of our cell set-up to grant access to the region of the electrode furthest to the electrode, and the low optical penetration depth of light in most battery materials, we assess the most polarized part of the cell.

After 1C cycling, the reflectance increases more significantly than after 0.15C cycling (Fig. 5(b and c)): peak changes at 500 nm are 0.06% (0.15C) *versus* 0.11% (1C), indicating higher intra-particle lithium concentration gradients from kinetic limitations at higher rates. Two other key observations emerge: first, a greater wavelength spread occurs after the 1C relaxation due to the electrode being at higher SoC, where wavelength responses diverge more (the discharge capacity after the 0.15C relaxation is 187 mAh g^{-1}, while that after the 1C relaxation is 140 mAh g^{-1}). Secondly, the reflectance during the 0.15C relaxation continues to increase across the entire 5 h OCV period (Fig. 5(b)) while the reflectance during the 1C relaxation begins to decrease after 1 h (Fig. 5(c)). The voltage during this OCV period does not decrease during this period (Fig. S26). We provide repeats for our experiments in a different cell in

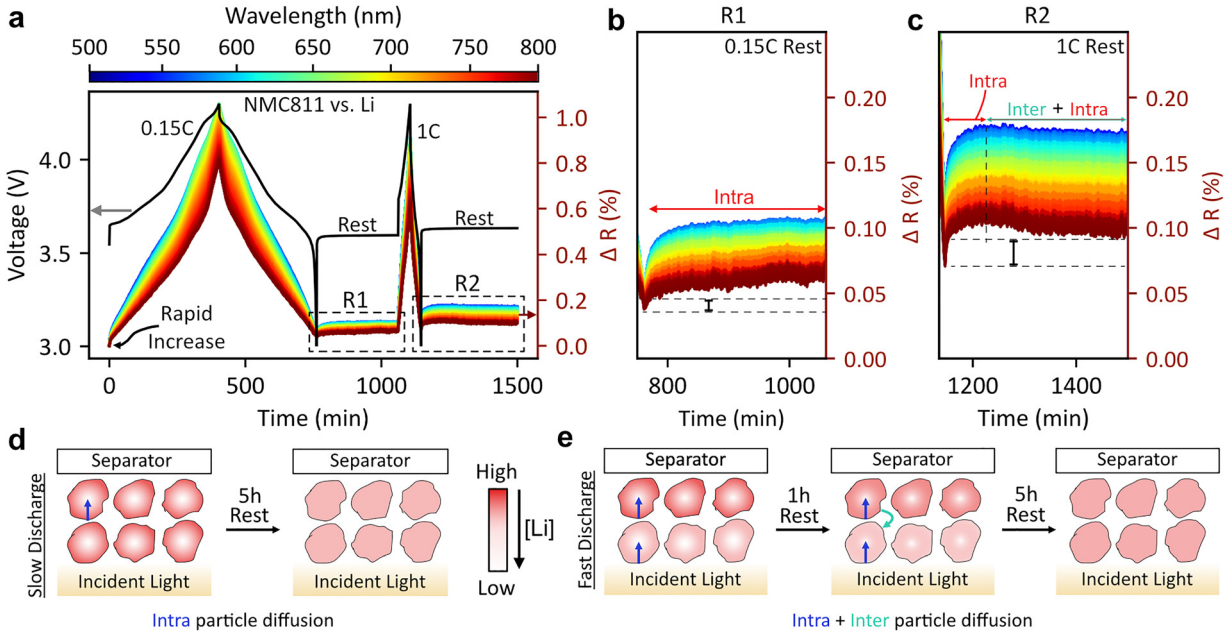

Fig. 5 Observing relaxation dynamics in NMC811 particles using DRS. (a) Two charge discharge sequences followed by a 5 h rest period of NMC811 at 0.15C and 1C respectively. During the rest period, an increase in reflectance at all wavelengths is seen, with a more pronounced effect after the 1C discharge, due to the greater extent of polarization in the cell. This can be explained by poor solid-state lithium-ion diffusion in the fully lithiated state. (b) Zoomed in relaxation profile during the relaxation following the 0.15C discharge. The increase in reflectance can be explained by intra-particle relaxation, as demonstrated in the scheme on the bottom left (c) Zoomed in relaxation profile during the relaxation following the 1C discharge. An increase and then decrease in reflectance is seen, which is due to combined inter and intra particle relaxation. (d) A schematic showing processes which occur after a slow discharge, mainly intra particle diffusion. (e) A schematic showing processes which occur after a fast discharge, which are a combination of inter and intra particle diffusion.

Fig. S24, highlighting the same 'dip' in reflectance during the OCV period after fast discharges. We also observe the same dip in reflectance during an OCV rest of an LFP–Li cell after a fast 5C discharge (Fig. S25). We propose that in addition to the intra-particle Li redistribution, there is a second inter-particle redistribution which we attribute to differences in SoC at the top and bottom of the electrode (see schematic in the bottom right corner of Fig. 5). At 1C discharge, the particles close to the separator membrane are more lithiated than the bottom region (which is monitored by DRS) due to limited ionic diffusion across the depth of the electrode as discussed in the rate tests. Therefore, we believe that in the first hour of relaxation, the reflectance increases due to inter-particle Li redistribution from the surface to the core. Subsequently, the reflectance decreases for the next 4 hours as the bottom particles receive Li ions from particles closer to the separator as intra-particle Li equilibrium takes place. We note that we have already used cross-sectional confocal microscopy to validate the existence of through-plane SoC gradients in LFP (Fig. S17), further validating our hypothesis. Thus, two competing processes occur: intra-particle relaxation which causes the reflectance to increase, and inter-particle relaxation which causes the reflectance to decrease. Designing better batteries requires the optimization of both material (solid state) and electrode (liquid) diffusion. While such processes have been studied previously by synchrotron X-ray and muon spectroscopy,[43,44] the use of DRS opens up new avenues for studying these processes at a fraction of the cost, allowing for multiscale characterization of batteries.

Operando DRS tracking of degradation processes

The kinetic limitations in solid state diffusion discussed above can lead to capacity losses in battery materials as it becomes difficult to fully insert/reinsert all of the lithium ions. We study this in the context of NMC811 cathodes and show that continued cycling at higher voltages can also induce capacity loss due to increased impedance from surface degradation.

NMC811-Li batteries often have a low coulombic efficiency in their initial cycles.[45] First cycle capacity losses have been ascribed to several reasons including side reactions,[46] loss of lithium inventory due to irreversible structural changes,[47] or slow diffusion at high degree of lithiation.[48] In Fig. 6(a) we perform continuous cycling of a cell which has been formed previously (two formation cycles at 0.2C), thus any capacity losses seen are not due to solid electrolyte interphase (SEI) formation. The capacity at each cycle can be found in Fig. S27(b). After the first cycle at 0.5C, a low coulombic efficiency of only 89% is seen. During the following cycle at 1C (charge up to 4.3 V), the CE improves to 96.7% before stabilizing at 99.85% for the next four cycles, which is maintained even after changing the upper cutoff voltage to 4.6 V.

However, from the reflectance *vs.* time plots in Fig. 6(a) it is apparent that the SoC of the electrode never returns to its

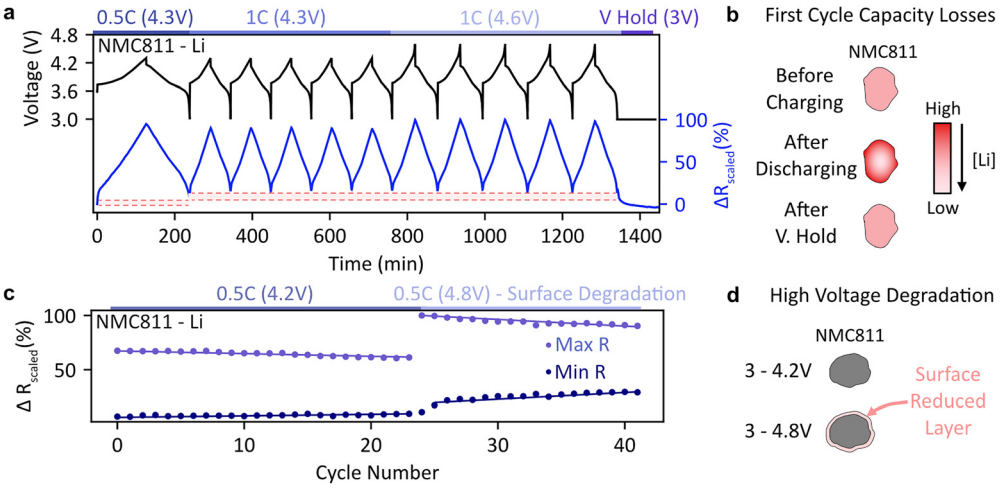

Fig. 6 Tracking the causes of degradation in Ni rich cathode materials. (a) Repeated charge/discharge of NMC811. After the first cycle, the reflectance does not return to its original value even after repeated cycling and increasing the upper cutoff voltage. (b) Only after performing a voltage hold at 3 V post-cycling does the reflectance return to its original value. (c) Reflectance *vs.* time at 500 nm for an NMC811 cell initially cycled between 3 and 4.2 V twenty-five times and subsequently between 3 and 4.8 V eighteen times. After the first few cycles to 4.2 V, the peak and minimum reflectance (black dashed arrows) remain roughly constant. However, when cycled to 4.8 V, both these values begin changing, reducing reversibility in the cathode. (d) This is due to the formation of a resistive surface reduced layer on the cathode surface at higher voltages.

original value after the first cycle. In a half-cell configuration where loss of lithium inventory is non-existent, this suggests a heterogeneity between the charging and discharging dynamics. This issue only occurs in the first two cycles (carried out at C/2 and 1C respectively), with subsequent 1C cycles showing reversible behaviour, pointing to lithium-ion diffusion problems during initial discharge. By performing a voltage hold at 3 V after 10 cycles we were able to decrease the value of reflectance to its original value and fully re-lithiate the cathode, overcoming the sluggish diffusion coefficient of NMC811 at this SoC (Fig. 6(b)). The capacity obtained after the voltage hold was 25 mAh g^{-1}, which is the same as the capacity lost after the first 0.5C cycle (20 mAh g^{-1}) and the second 1C cycle (5 mAh g^{-1}). This is consistent with previous reports of a drop in the diffusion coefficient of NMC811 at the end of discharge.[19,44]

In full cells, where capacity loss can originate from either electrode, DRS can be a powerful technique to understand which electrode is undergoing irreversible capacity loss. This analysis can be applied to a range of other materials as we demonstrate for TiO_2 anodes in Fig. S28 and Note S11. Moreover, in half-cells, such as the NMC811-Li system studied here side reactions can occur on the anode leading to impedance growth and lower coulombic efficiency. By acquiring reflected light from one electrode, we can selectively acquire information about the cathode independently of the anode.

The surface sensitivity of DRS could make it an interesting avenue to study surface/interphase engineering in high-nickel cathodes. For example, the addition of coatings, gradient structures, or elemental dopants will manifest as changes in the reflectance spectra and allow the tracking of changes in the oxidation state of transition metal dopant as shown when comparing the DRS spectra of NMC and LNO (Note S5).

Conclusions

In summary, we propose diffuse reflectance spectroscopy as a technique for the *operando* measurement of processes in battery electrodes. Compared to other *operando* analysis methods, DRS is an inexpensive method to capture subtle changes in the reflectance of the battery electrodes, allowing for high-throughput real-time battery screening. First, we demonstrate that DRS can be applied to a wide variety of battery materials and can visualize oxidation changes in materials containing Ni or Mn. Secondly, we show that DRS can be used to monitor lag in SoC near the current collector in thick electrodes. Third, DRS allows for the analysis of charge redistribution inside active particles as well as between different regions of the electrode. Finally, DRS allows for studying surface limited behaviour and tracking degradation mechanisms in next generation battery materials. This technique does not require any optics or active focusing systems, allowing for inexpensive implementation of this technique. This allows for both the democratization of battery material research and the mass-parallelisation of *operando* screening.

Methods

Diffuse reflectance spectroscopy setup

An integrating sphere with an integrated light source (Ocean Optics ISB-REF) and gloss trap was used to collect the reflectance spectra from batteries. The cell was mounted on the integrating sphere using a custom-built 3D printed mount, with magnetically attached spring loaded contact pins providing electrical connections (see Fig. S4).

The integrating sphere was connected to a CCD spectrometer (ST-VIS 25 μm, Ocean Optics) using an SMA optical fibre (Ocean Optics). The sphere was mounted on a cooling stage (Thorlabs PCT-1) with a feedback loop to ensure that the heat generated by the light source was dissipated. The temperature of the stage was maintained at 19 °C for all experiments.

Fabrication of optical cells

LFP and LMO were obtained from MTI Corporation. TiO_2 was obtained from Sigma Aldrich. Polycrystalline NMC811 was obtained from Lifun. Single crystal NMC811 was synthesised according to a co-precipitation procedure.[49]

Free-standing electrodes were used for all optical cells. Usually, 400 mg of active material and 50 mg of carbon black were ground together using a mortar and pestle. For TiO_2, 250 mg of active material, 150 mg of PVDF and 100 mg of Super P was used. Then, 50 mg of 6 wt% PVDF was added, and the entire mixture was mixed in a Thinky mixer for 10 minutes until a homogenous mixture was formed. The slurry was then blade coated on a glass plate (wet film thickness between 200–270 μm) and slowly dried at 65 °C to form a film. A low temperature must be used for this step as fast evaporation of the solvent can lead to electrode cracking due to the inflexibility of the glass substrate. Once the electrodes were dry, a single-edged razor blade was used to pry the electrode off the glass surface. Electrode disks of 12 or 13 mm were then punched out of the film. The electrodes were dried in a 120 °C vacuum oven prior to cell assembly.

To make an optical cell in a transmissive configuration, a 15 mm glass window (1.1 mm thick, Biolin Scientific) with 190 nm of FTO coating (surface resistivity 6–8 ohm sq.$^{-1}$) was used as the optical window/current collector. It was stuck to a coin cell can with a 12 mm hole cut out (obtained from Cambridge Energy Solutions) by melting a ring-shaped thermoplastic sealant (Dupont Surlyn™) at 120 °C. An aluminium ring was placed on the FTO glass (inner diameter 13 mm, outer diameter 19 mm). Thus, when the coin cell was crimped, the aluminium foil was pressed between the surface of the FTO glass and the can, enabling electrical connection. The free-standing electrode was placed in the central hole of the ring, and the coin cell was assembled as normal with electrolyte, a lithium chip, 0.2 mm spacer, spring, and cap. After crimping, solvent resistant potting epoxy (Electrolube) was applied to the outside of the coin cell (between the glass window and cell can) for additional sealing, as the thermoplastic is not completely impervious to moisture. The cell was rested for at least 12 h to allow for epoxy curing and electrolyte infiltration. Finally, an annular ring composed of black masking tape (Thorlabs) with an outer diameter of 20 mm and inner diameter of 8 mm was paced on the windowed side of the cell to optically mask all non-active components (steel casing, dried epoxy).

To make an optical cell in a non-transmissive configuration, a 13 mm diameter borosilicate glass circle (0.5 mm thickness, Cambridge Energy Solutions) was attached to the surface of a coin cell can (with a 10 mm hole cutout, obtained from Cambridge Energy Solutions) as described earlier. A freestanding electrode (13 mm diameter) was placed on the glass window and a few drops of electrolyte added to ensure adherence of the electrode to the glass window. Then, an aluminium mesh (Goodfellow, nominal aperture: 0.11 mm, wire diameter: 0.1 mm) was cut into a 19 mm disc and placed on top of the freestanding current collector. The cell was then assembled as previously, but with a 0.5 mm spacer due to the reduced thickness of the glass window, with epoxy applied to the outside upon completion. A detailed description of cell assembly can also be found in our prior publication.[26] The annular masking tape ring was applied as before.

Due to the limited deflection of the thick glass used in the coin cell (either 0.5 mm or 1.1 mm) the windows can be treated as rigid spacers. The thickness of the metal spacers used beneath the cell spring were adjusted to ensure that the total thickness of spacers in the cell lay between 1.0–1.3 mm. As the electrodes are placed between two mechanically rigid plates, they are immobilized with respect to the window, ensuring that the same mechanical constraints as a conventional coin cell are maintained.

For the experiments with the rate dependency of thick and thin LFP electrodes, all experiments were carried out in a transmissive configuration, while all other experiments were carried out in a non-transmissive configuration.

Spectroelectrochemical characterization

Electrochemical cycling was carried out using a Biologic BCS-805 potentiostat. High reflectance PTFE Sheets (Thorlabs) were used as the reflectance standard. First, the reflectance spectrum of the reference was collected using an integration time of 3 ms. Then, the reflectance spectrum of the battery was obtained at an integration time of 50 ms. Assuming a linear correlation between light intensity and integration time, all spectra were divided by a scaling factor corresponding to the ratio of integration times (50/3). Data from the spectrometer and potentiostat were saved as.txt files. Python scripts were used to synchronize the time between both sets of data, and for data analysis. A Savitzky–Golay filter with a window size of 21 and polynomial order of 5 was used for smoothening the data prior to plotting. Either 240 or 600 scans were averaged, corresponding to an acquisition time of 12 s or 30 s (used depending on the charging rate).

Operando cross-sectional microscopy

Confocal cross-sectional microscopy was carried out as previously reported.[21,50,51] A commercial *operando* optical cell (LaserTec Co.) was used for all measurements. First, the anode, separator, and cathode were clamped together using a spring-loaded clamp in the glovebox. A cross-section was obtained by slicing the cell components using a microtome. The electrolyte (same as coin cell) was filled with vacuum infiltration in the antechamber of the glovebox. Finally, a polymeric filler material was applied to prevent excessive electrode accumulation at the surface of the cross-section, which could impair optical observation. The entire assembly was sealed using an O-ring and quartz window. Confocal images were obtained through a

commercial, white-light microscope (Lasertec Co. ECCS B-320). The image acquisition time was approximately 30 seconds. A Biologic VMP-3 potentiostat was used for all *operando* cycling.

Author contributions

A. P. conceived the idea, built the setup, and performed all experiments, and analysed the data. G. K. assisted in data collection and analysis. H. J. T. synthesized the NMC811 particles. A. I. and H. A. supervised the confocal microscopy. M. D. V. supervised the project and acquired funding. A. P. and M. D. V. wrote the manuscript, and all authors reviewed it.

Conflicts of interest

There are no conflicts of interest to declare.

Data availability

The data underlying this paper can be found at the University of Cambridge online repository [https://doi.org/10.17863/CAM.129500]. Supplementary information: Supplementary Fig. S1–S28 and Supplementary Notes S1–S11 which describe additional considerations for DRS spectroscopy of battery and data supporting the conclusions in the main text.

Supplementary information (SI) available. See DOI: https://doi.org/10.1039/d6ee00376a.

Acknowledgements

A.P. and M.D.V. acknowledge support from the ERC Consolidator Grant (MIGHTY, 866005). AP acknowledges the support of the Japanese Society for the Promotion of Science (JSPS) Summer Program 2024, the UKRI NanoDTC EP/S022953/1, the Cambridge Commonwealth and International Trust, the Cambridge Philosophical Society Research Studentship, and Prof. Neil Greenham & Prof. Clare Grey for insightful discussions. G. K. acknowledges support from the Engineering and Physical Sciences Research Council Centre for Doctoral Training in Sensor Technologies for a Healthy and Sustainable Future [EP/S023046/1]. H.A. and M.D.V. acknowledge support from the JST ASPIRE program JPMJAP2047. A.P., H.A., A.I., and M.D.V. thank Lasertec Co. for providing access to the ECCS-B320 block cell as well as Atsuko Yaguchi, Yoshihiro Nishimura, and Yuya Akimoto (Lasertec Co.) for experimental assistance. For the purpose of Open Access, the authors have applied a Creative Commons Attribution (CC BY) license to any Author Accepted Manuscript version arising from this submission.

References

1 E. S. Takeuchi, A. C. Marschilok, K. J. Takeuchi, A. Ignatov, Z. Zhong and M. Croft, Energy dispersive X-ray diffraction of lithium–silver vanadium phosphorous oxide cells: *in situ* cathode depth profiling of an electrochemical reduction–displacement reaction, *Energy Environ. Sci.*, 2013, **6**(5), 1465–1470, DOI: 10.1039/C3EE40152A.

2 P. Pietsch, M. Hess, W. Ludwig, J. Eller and V. Wood, Combining *operando* synchrotron X-ray tomographic microscopy and scanning X-ray diffraction to study lithium ion batteries, *Sci. Rep.*, 2016, **6**(1), 27994, DOI: 10.1038/srep27994.

3 P. Black, A. Sorrentino, F. Fauth, I. Yousef, L. Simonelli, C. Frontera, A. Ponrouch, D. Tonti and M. Rosa Palacín, Synchrotron radiation based *operando* characterization of battery materials, *Chem. Sci.*, 2023, **14**(7), 1641–1665, DOI: 10.1039/D2SC04397A.

4 O. Pecher, J. Carretero-González, K. J. Griffith and C. P. Grey, Materials' methods: NMR in battery research, *Chem. Mater.*, 2017, **29**(1), 213–242, DOI: 10.1021/acs.chemmater.6b03183.

5 B. Key, R. Bhattacharyya, M. Morcrette, V. Seznéc, J.-M. Tarascon and C. P. Grey, Real-time NMR investigations of structural changes in silicon electrodes for lithium-ion batteries, *J. Am. Chem. Soc.*, 2009, **131**(26), 9239–9249, DOI: 10.1021/ja8086278.

6 C. P. Grey and N. Dupré, NMR studies of cathode materials for lithium-ion rechargeable batteries, *Chem. Rev.*, 2004, **104**(10), 4493–4512, DOI: 10.1021/cr020734p.

7 W. M. Dose, W. Li, I. Temprano, C. A. O'Keefe, B. L. Mehdi, M. F. L. De Volder and C. P. Grey, Onset potential for electrolyte oxidation and Ni-rich cathode degradation in lithium-ion batteries, *ACS Energy Lett.*, 2022, **7**(10), 3524–3530, DOI: 10.1021/acsenergylett.2c01722.

8 R. Jung, M. Metzger, F. Maglia, C. Stinner and H. A. Gasteiger, Oxygen release and its effect on the cycling stability of $LiNi_xMn_yCo_zO_2$ (NMC) cathode materials for Li-ion batteries, *J. Electrochem. Soc.*, 2017, **164**(7), A1361, DOI: 10.1149/2.0021707jes.

9 A. Gajan, C. Lecourt, B. E. Torres Bautista, L. Fillaud, J. Demeaux and I. T. Lucas, Solid electrolyte interphase instability in operating lithium-ion batteries unraveled by enhanced-Raman spectroscopy, *ACS Energy Lett.*, 2021, **6**(5), 1757–1763, DOI: 10.1021/acsenergylett.1c00436.

10 A. Krause, O. Tkacheva, A. Omar, U. Langklotz, L. Giebeler, S. Dörfler, F. Fauth, T. Mikolajick and W. M. Weber, *In situ* Raman spectroscopy on silicon nanowire anodes integrated in lithium ion batteries, *J. Electrochem. Soc.*, 2019, **166**(3), A5378, DOI: 10.1149/2.0541903jes.

11 P. Lanz and P. Novák, Combined *in situ* Raman and IR microscopy at the interface of a single graphite particle with ethylene carbonate/dimethyl carbonate, *J. Electrochem. Soc.*, 2014, **161**(10), A1555, DOI: 10.1149/2.0021410jes.

12 V. Stancovski and S. Badilescu, *In situ* Raman spectroscopic–electrochemical studies of lithium-ion battery materials: a historical overview, *J. Appl. Electrochem.*, 2014, **44**(1), 23–43, DOI: 10.1007/s10800-013-0628-0.

13 E. Miele, W. M. Dose, I. Manyakin, M. H. Frosz, Z. Ruff, M. F. L. De Volder, C. P. Grey, J. J. Baumberg and T. G. Euser, Hollow-core optical fibre sensors for *operando* raman spectroscopy investigation of Li-ion battery liquid

electrolytes, *Nat. Commun.*, 2022, **13**(1), 1651, DOI: 10.1038/s41467-022-29330-4.

14 M. Yousaf, U. Naseer, Y. Li, Z. Ali, N. Mahmood, L. Wang, P. Gao and S. Guo, A mechanistic study of electrode materials for rechargeable batteries beyond lithium ions by *in situ* transmission electron microscopy, *Energy Environ. Sci.*, 2021, **14**(5), 2670–2707, DOI: 10.1039/D0EE03295F.

15 J. Wu, M. Fenech, R. F. Webster, R. D. Tilley and N. Sharma, Electron microscopy and its role in advanced lithium-ion battery research, *Sustainable Energy Fuels*, 2019, **3**(7), 1623–1646, DOI: 10.1039/C9SE00038K.

16 Y. Yuan, K. Amine, J. Lu and R. Shahbazian-Yassar, Understanding materials challenges for rechargeable ion batteries with *in situ* transmission electron microscopy, *Nat. Commun.*, 2017, **8**(1), 15806, DOI: 10.1038/ncomms15806.

17 P. van Helden, The cost of research in developing countries, *EMBO Rep.*, 2012, **13**(5), 395, DOI: 10.1038/embor.2012.43.

18 A. J. Merryweather, Q. Jacquet, S. P. Emge, C. Schnedermann, A. Rao and C. P. Grey, *Operando* monitoring of single-particle kinetic state-of-charge heterogeneities and cracking in high-rate Li-ion anodes, *Nat. Mater.*, 2022, **21**(11), 1306–1313, DOI: 10.1038/s41563-022-01324-z.

19 C. Xu, A. J. Merryweather, S. S. Pandurangi, Z. Lun, D. S. Hall, V. S. Deshpande, N. A. Fleck, C. Schnedermann, A. Rao and C. P. Grey, *Operando* visualization of kinetically induced lithium heterogeneities in single-particle layered Ni-rich cathodes, *Joule*, 2022, **6**(11), 2535–2546, DOI: 10.1016/j.joule.2022.09.008.

20 R. Pandya, L. Valzania, F. Dorchies, F. Xia, J. Mc Hugh, A. Mathieson, H. J. Tan, T. G. Parton, L. Godeffroy, K. Mazloomian, T. S. Miller, F. Kanoufi, M. De Volder, J.-M. Tarascon, S. Gigan, H. B. de Aguiar and A. Grimaud, Three-dimensional *operando* optical imaging of particle and electrolyte heterogeneities inside Li-ion batteries, *Nat. Nanotechnol.*, 2023, **18**(10), 1185–1194, DOI: 10.1038/s41565-023-01466-4.

21 H. Arai, A. Yaguchi, Y. Nishimura, Y. Akimoto and A. Ikezawa, *Operando* optical analysis of $LiFePO_4$ composite electrodes, *J. Phys. Chem. C*, 2021, **125**(7), 3776–3780, DOI: 10.1021/acs.jpcc.0c11156.

22 M. Ménétrier, I. Saadoune, S. Levasseur and C. Delmas, The insulator–metal transition upon lithium deintercalation from $LiCoO_2$: electronic properties and 7Li NMR study, *J. Mater. Chem.*, 1999, **9**(5), 1135–1140, DOI: 10.1039/A900016J.

23 A. Pujari, K. Raju, A. Yaguchi, Y. Nishimura, Y. Akimoto, A. Ikezawa, H. Arai and M. D. Volder, *Operando* confocal microscopy of structured battery electrodes, *J. Electrochem. Soc.*, 2025, **172**(7), 070514, DOI: 10.1149/1945-7111/ade936.

24 J. Hedman, D. Nilebo, E. Larsson Langhammer and F. Björefors, Fibre optic sensor for characterisation of lithium-ion batteries, *ChemSusChem*, 2020, **13**(21), 5731–5739, DOI: 10.1002/cssc.202001709.

25 J. Hedman and F. Björefors, Fiber optic monitoring of composite lithium iron phosphate cathodes in pouch cell batteries, *ACS Appl. Energy Mater.*, 2022, **5**(1), 870–881, DOI: 10.1021/acsaem.1c03304.

26 A. Pujari, B. Kim, N. C. Greenham and M. De Volder, Identifying current collectors that enable light–battery interactions, *Small Methods*, 2024, **8**(10), 2301572, DOI: 10.1002/smtd.202301572.

27 A. Pujari, A. J. Merryweather and C. Schnedermann, Optimal coin cell design for *operando* optical characterisation of lithium-ion batteries, *J. Electrochem. Soc.*, 2026, **173**(1), 010505, DOI: 10.1149/1945-7111/ae2f9e.

28 A. Erraji, R. Masrour and L. Xu, *Ab initio* study of $LiMn_2O_4$ cathode: electrochemical and optical properties for Li-ion batteries and optoelectronic devices, *Ionics*, 2024, **30**(12), 7917–7928, DOI: 10.1007/s11581-024-05841-6.

29 M. K. Kinyanjui, P. Axmann, M. Wohlfahrt-Mehrens, P. Moreau, F. Boucher and U. Kaiser, Origin of valence and core excitations in $LiFePO_4$ and $FePO_4$, *J. Phys.: Condens. Matter*, 2010, **22**(27), 275501, DOI: 10.1088/0953-8984/22/27/275501.

30 A. Lee, M. Vörös, W. M. Dose, J. Niklas, O. Poluektov, R. D. Schaller, H. Iddir, V. A. Maroni, E. Lee, B. Ingram, L. A. Curtiss and C. S. Johnson, Photo-accelerated fast charging of lithium-ion batteries, *Nat. Commun.*, 2019, **10**(1), 4946, DOI: 10.1038/s41467-019-12863-6.

31 S. T. Lee, K. Raveendranath, M. R. Tomy, M. Paulraj, S. Jayalekshmi and J. Ravi, Evidence of band structure modification of $LiMn_2O_4$ upon lithium deintercalation by photoacoustic spectroscopy, *Appl. Phys. Lett.*, 2007, **90**(16), 161912, DOI: 10.1063/1.2728033.

32 Y. Joshi, E. Hadjixenophontos, S. Nowak, R. Lawitzki, P. K. Ghosh and G. Schmitz, Modulation of the optical properties of lithium manganese oxide *via* Li-ion de/intercalation, *Adv. Opt. Mater.*, 2018, **6**(12), 1701362, DOI: 10.1002/adom.201701362.

33 Y. Joshi, R. Lawitzki and G. Schmitz, Slow-moving phase boundary in $Li_{4/3}$ + $Ti_{5/3}O_4$, *Small Methods*, 2021, **5**(10), 2100532, DOI: 10.1002/smtd.202100532.

34 S. Banifarsi, Y. Joshi, R. Lawitzki, G. Csiszár and G. Schmitz, Optical modulation and phase distribution in $LiCoO_2$ upon Li-ion de/intercalation, *J. Electrochem. Soc.*, 2022, **169**(4), 046509, DOI: 10.1149/1945-7111/ac63f6.

35 Y. Zhang, J. A. Alarco, A. S. Best, G. A. Snook, P. C. Talbot and J. Y. Nerkar, Re-evaluation of experimental measurements for the validation of electronic band structure calculations for $LiFePO_4$ and $FePO_4$, *RSC Adv.*, 2019, **9**(2), 1134–1146, DOI: 10.1039/C8RA09154D.

36 T. Kim, W. Choi, H.-C. Shin, J.-Y. Choi, J. M. Kim, M.-S. Park and W.-S. Yoon, Applications of voltammetry in lithium ion battery research, *J. Electrochem. Sci. Technol*, 2020, **11**(1), 14–25, DOI: 10.33961/jecst.2019.00619.

37 M. Wagemaker, D. Lützenkirchen-Hecht, A. A. van Well and R. Frahm, Atomic and electronic bulk *versus* surface structure: lithium intercalation in anatase TiO_2, *J. Phys. Chem. B*, 2004, **108**(33), 12456–12464, DOI: 10.1021/jp048567f.

38 T. Facci and F. Huguenin, Spectroelectrochemical properties and lithium ion storage in self-assembled nanocomposites from TiO_2, *Langmuir*, 2010, **26**(6), 4489–4496, DOI: 10.1021/la903301c.

39 C. J. Dahlman, S. Heo, Y. Zhang, L. C. Reimnitz, D. He, M. Tang and D. J. Milliron, Dynamics of lithium insertion in electrochromic titanium dioxide nanocrystal ensembles, *J. Am. Chem. Soc.*, 2021, **143**(22), 8278–8294, DOI: 10.1021/jacs.0c10628.

40 R. Li, X. Ma, J. Li, J. Cao, H. Gao, T. Li, X. Zhang, L. Wang, Q. Zhang, G. Wang, C. Hou, Y. Li, T. Palacios, Y. Lin, H. Wang and X. Ling, Flexible and high-performance electrochromic devices enabled by self-assembled 2D TiO_2/MXene heterostructures, *Nat. Commun.*, 2021, **12**(1), 1587, DOI: 10.1038/s41467-021-21852-7.

41 M. Wagemaker, D. Lützenkirchen-Hecht, A. A. van Well and R. Frahm, Atomic and electronic bulk *versus* surface structure: lithium intercalation in anatase TiO_2, *J. Phys. Chem. B*, 2004, **108**(33), 12456–12464, DOI: 10.1021/jp048567f.

42 N. J. J. de Klerk, A. Vasileiadis, R. B. Smith, M. Z. Bazant and M. Wagemaker, Explaining key properties of lithiation in TiO_2-anatase Li-ion battery electrodes using phase-field modeling, *Phys. Rev. Mater.*, 2017, **1**(2), 025404, DOI: 10.1103/PhysRevMaterials.1.025404.

43 S. Park, K. Kameyama and T. Yao, Relaxation crystal analysis of $LiFePO_4$ cathode for Li-ion secondary battery, *Electrochem. Solid-State Lett.*, 2012, **15**(4), A49, DOI: 10.1149/2.012204esl.

44 I. McClelland, S. G. Booth, N. N. Anthonisamy, L. A. Middlemiss, G. E. Pérez, E. J. Cussen, P. J. Baker and S. A. Cussen, Direct observation of dynamic lithium diffusion behavior in nickel-rich, $LiNi_{0.8}Mn_{0.1}Co_{0.1}O_2$ (NMC811) cathodes using *operando* muon spectroscopy, *Chem. Mater.*, 2023, **35**(11), 4149–4158, DOI: 10.1021/acs.chemmater.2c03834.

45 K. Egorov, W. Zhao, K. Knemeyer, A. N. Filippin, A. Giraldo and C. Battaglia, Mitigating first-cycle capacity losses in NMC811 *via* lithicone layers grown by molecular layer deposition, *ACS Appl. Mater. Interfaces*, 2023, **15**(16), 20075–20080, DOI: 10.1021/acsami.2c23158.

46 F. Zhang, S. Lou, S. Li, Z. Yu, Q. Liu, A. Dai, C. Cao, M. F. Toney, M. Ge, X. Xiao, W.-K. Lee, Y. Yao, J. Deng, T. Liu, Y. Tang, G. Yin, J. Lu, D. Su and J. Wang, Surface regulation enables high stability of single-crystal lithium-ion cathodes at high voltage, *Nat. Commun.*, 2020, **11**(1), 3050, DOI: 10.1038/s41467-020-16824-2.

47 X. Fan, G. Hu, B. Zhang, X. Ou, J. Zhang, W. Zhao, H. Jia, L. Zou, P. Li and Y. Yang, Crack-free single-crystalline Ni-rich layered NCM cathode enable superior cycling performance of lithium-ion batteries, *Nano Energy*, 2020, **70**, 104450, DOI: 10.1016/j.nanoen.2020.104450.

48 H. Zhou, F. Xin, B. Pei and M. S. Whittingham, What limits the capacity of layered oxide cathodes in lithium batteries?, *ACS Energy Lett.*, 2019, **4**(8), 1902–1906, DOI: 10.1021/acsenergylett.9b01236.

49 H. J. Tan, C. P. Grey and M. De Volder, Study of particle size distribution effects in battery electrodes using monodisperse NMC cathode particles, *J. Electrochem. Soc.*, 2025, **172**(10), 100533, DOI: 10.1149/1945-7111/ae0f56.

50 A. Pujari, K. Raju, A. Yaguchi, Y. Nishimura, Y. Akimoto, A. Ikezawa, H. Arai and M. D. Volder, *Operando* confocal microscopy of structured battery electrodes, *J. Electrochem. Soc.*, 2025, **172**(7), 070514, DOI: 10.1149/1945-7111/ade936.

51 A. Pujari, B.-M. Kim, F. N. Sayed, K. Sanders, W. M. Dose, A. Mathieson, C. P. Grey, N. C. Greenham and M. De Volder, Does heat play a role in the observed behavior of aqueous photobatteries?, *ACS Energy Lett.*, 2023, **8**(11), 4625–4633, DOI: 10.1021/acsenergylett.3c01627.

